




# Single crystal growth and properties of the polar ferromagnet $\text{Mn}_{1.05}\text{Bi}$ with Kagome layers, huge magnetic anisotropy and slow spin dynamics

Quinn D. Gibson <sup>1</sup>, Craig M. Robertson,<sup>1</sup> Matthew S. Dyer <sup>1</sup>, Marco Zanella <sup>1</sup>, T. Wesley Surta <sup>1</sup>, Luke M. Daniels <sup>1</sup>,  
John B. Claridge <sup>1</sup>, Jonathan Alaria <sup>2</sup> and Matthew J. Rosseinsky<sup>1,\*</sup>

<sup>1</sup>University of Liverpool Department of Chemistry, Crown Street, Liverpool, L69 7ZD, United Kingdom

<sup>2</sup>University of Liverpool Department of Physics, Oliver Lodge Laboratory, Liverpool, L69 7ZE, United Kingdom

 (Received 30 June 2022; revised 16 September 2022; accepted 20 September 2022; published 18 November 2022)

The synthesis, structure, and properties of single crystalline  $\text{Mn}_{1.05}\text{Bi}$  in the polar space group  $Fdd2$  are reported.  $\text{Mn}_{1.05}\text{Bi}$  is isostructural to the previously reported  $\text{Mn}_{1.05}\text{Rh}_{0.02}\text{Bi}$ , with both ordered interstitials and ordered vacancies of Mn leading to Kagome-like layers. The ordering of the interstitials breaks inversion symmetry and forces the material into a polar space group. DC magnetization reveals ferromagnetic properties with a huge magnetic anisotropy, with the magnetization pinned along the  $a$  axis (the stacking axis), and multiple magnetic transitions which retain this anisotropy. AC measurements confirm these transitions and show very sluggish spin dynamics along the  $a$  axis, with a very large temperature-dependent out-of-phase response. Heat-capacity measurements reveal the presence of Schottky defects, and resistivity measurement confirms the transitions and reveal the material to be dominated by magnetic scattering. Overall,  $\text{Mn}_{1.05}\text{Bi}$  shows magnetic properties markedly different from hexagonal, NiAs-type MnBi, driven by ordered interstitials and vacancies of Mn, stabilizing a likely complex magnetic structure with strongly temperature-dependent spin dynamics. This is supported by density-functional theory calculations, which suggest a strongly anisotropic noncollinear ground state driven by Kagome layers and asymmetric Mn environments.

DOI: [10.1103/PhysRevMaterials.6.114405](https://doi.org/10.1103/PhysRevMaterials.6.114405)

## I. INTRODUCTION

Metallic magnetic materials have seen a recent increase in interest, due to their ability to host combinations of non-collinear magnetic states and Weyl and Dirac fermions, leading to novel properties such as skyrmions and the topological Hall effect. Materials such as  $\text{Fe}_3\text{Sn}_2$  [1],  $\text{FeSn}$  [2],  $\text{CoSn}$  [3], and  $\text{TbMn}_6\text{Sn}_6$  [4] and  $\text{YMn}_6\text{Sn}_6$  [5] take advantage of Kagome networks of magnetic ions to generate noncollinear spin structures and Dirac electrons, with the noncollinear magnet  $\text{Mn}_3\text{Sn}$  showing similar effects [6], and materials such as  $\text{MnSi}$  which lack inversion centers have asymmetric exchange leading to the realization of skyrmions on the surface [7,8]. The interplay of mobile electrons, spin-orbit coupling, and noncollinear magnetic structures leads in general to novel magnetoelectric effects, meriting reinvestigation into metallic materials consisting of  $3d$  transition metals and  $p$ -block elements with structures that can host noncollinear magnetic states.

However, there are very few materials that contain bonds between magnetic  $3d$  transition metals and the heaviest  $p$ -block element, Bi—for example, Fe and Co intermetallics with Bi can only be formed under high pressure [9,10], and no binary intermetallic between Cr and Bi has been reported. Mn is an exception to this rule, and materials that contain both Mn and Bi are of particular interest, as they combine the strong localized magnetism of Mn with the large spin-orbit

coupling of Bi. Examples of these include the quasi-1D material  $\text{KMn}_6\text{Bi}_5$  [11] that becomes superconducting upon the application of pressure [12], the  $\text{MnBi}_2\text{Te}_4$ - $\text{Bi}_2\text{Te}_3$  family of materials that exhibit both antiferromagnetic [13,14] and ferromagnetic [13] topological insulating states and the  $\text{AMnBi}_2$  ( $A =$  alkaline earth, Eu, Yb) family of materials that combine Dirac-dispersion generating Bi nets and magnetic Mn-Bi layers [14–16]. Furthermore there are the Mn-Bi analogs of Fe-As superconductors [17] which show large magnetoresistance [18], the quasi-1D material  $\text{Ti}_4\text{MnBi}_2$  which is an incipient antiferromagnet [19].

The simplest MnBi material is the hexagonal intermetallic magnet MnBi, which first garnered interest as a rare-earth free room-temperature permanent magnet [20]. MnBi undergoes a spin reorientation starting at 140 K and finishing at 90 K, from having the easy axis along the stacking direction to the in-plane direction, wherein an associated lattice distortion kicks in and the material goes from hexagonal to orthorhombic [21]. During this spin reorientation, it has been reported to have a conical spin orientation which leads to a topological Hall effect [22]. MnBi has also been reported to have nonsaturating linear magnetoresistance [23] and Nernst effect [24]. MnBi has a structurally and compositionally closely related, high-temperature metastable Mn-rich relative referred to as “ $\text{Mn}_{1.1}\text{Bi}$ ” or “ $\text{Mn}_{1.08}\text{Bi}$ ,” which has been reported in various orthorhombic space groups and a suggested noncollinear magnetic structure from 230 to 0 K when quenched or doped with small amounts of stabilizing elements [25–30]. However, the structure of what is referred to by  $\text{Mn}_{1.1}\text{Bi}$  has not been conclusively studied, and studies of the properties of single

\*m.j.rosseinsky@liverpool.ac.uk

crystals of the material are limited to a study of the saturation magnetization and uniaxial anisotropy energy as a function of temperature [26].

Here we demonstrate the single crystal growth of metastable orthorhombic  $\text{Mn}_{1.05}\text{Bi}$ , its structure solution, and properties. We show that the metastable arrangement of defects leads to inversion symmetry breaking (leading to a polar structure), formation of Kagome layers, and to exchange pathways that result in magnetic properties markedly different from the parent material across the whole temperature range measured. Orthorhombic  $\text{Mn}_{1.05}\text{Bi}$  shows frustrated and slow spin dynamics as well as huge magnetic anisotropy, with the magnetization effectively pinned along the stacking axis of the pseudo-NiAs-type layers. This huge magnetic anisotropy is similar to that seen in thin films of the polar ferromagnetic metal FePt [31]. These features together establish  $\text{Mn}_{1.05}\text{Bi}$  as a ferromagnetic, polar metal at room temperature, for which there are very few material realizations. Density-functional theory calculations suggest the ground state is a highly anisotropic noncollinear state, consistent with experimental observations. Single crystalline  $\text{Mn}_{1.05}\text{Bi}$  thus represents a good candidate for the observation of noncollinear spin dynamics and the topological Hall effect. It illustrates that control of nonstoichiometric metastable defect compositions leads to the manipulation of magnetic ground states in pure binary intermetallic magnets. The fact that single crystals of  $\text{Mn}_{1.05}\text{Bi}$  can be grown and have these properties demonstrates that these vastly different properties from  $\text{MnBi}$  can be achieved through only tuning the Mn:Bi ratio, in contrast to the introduction of a third element as in  $\text{Mn}_{1.05}\text{Rh}_{0.02}\text{Bi}$ .

## II. MATERIALS AND METHODS

Crystals of  $\text{Mn}_{1.05}\text{Bi}$  were grown by self-flux method with excess Bi. Mn and Bi chunks were loaded in a 1:8 ratio in a 5-g batch in a carbon-coated evacuated quartz ampoule with a quartz wool plug. Mn chunks were precleaned by heating to 1000 °C in an evacuated quartz ampoule sandwiched between quartz wool. The sample was heated to 800 °C and slowly cooled to 430 °C at 0.1 °C/min, then removed from the furnace and centrifuged quickly at room temperature for 5 s, then quenched in water.

Single crystal x-ray diffraction (SXRD) was performed on a Bruker Venture D8 diffractometer using a Mo source. A small single crystal, broken off of a larger pseudohexagonal, was loaded using Parabar oil. The structure was solved using SHELXT [32] as implemented in Olex 2 [33].

Scanning electron microscopy (SEM) and energy-dispersive x-ray diffraction (EDX) were performed with a Hitachi S4800 instrument equipped with an EDX detector from Oxford instruments. Single crystals were loaded onto carbon tape attached to an alumina stub and coated with a thin film of carbon before performing imaging and EDX. Chemical quantification was performed using AZTEC software. EDX correction factors, for the different elements, were estimated by measuring the EDX spectra of appropriate standards. No metals other than Mn and Bi were observed in this analysis.

Resistivity measurements were performed on a Quantum Design physical properties measurement system (QD-PPMS)

using the four-probe method and a DC applied current. Heat-capacity measurements were performed on a QD-PPMS using the relaxation method, with a 32-mg crystal of  $\text{Mn}_{1.05}\text{Bi}$  attached to the heat-capacity puck using temperature-resistant N grease. This was also repeated with H grease at higher temperatures.

Magnetic measurements were performed on a Quantum Design magnetic properties measurement system (QD-MPMS), with the easy axis ( $a$  axis) determined by an applied field.

Density-functional theory calculations were performed with the Vienna *Ab initio* Simulation Package (VASP) [34]. The Mn  $3p$ ,  $3d$ , and  $4s$  and Bi  $5d$ ,  $6s$ , and  $6p$  electrons were considered as valence electrons with core electrons treated using the projector augmented-wave approach [35,36]. The Perdew-Burke-Ernzerhof (PBE) functional [37] was used, with a plane-wave cutoff energy of 400 eV and an  $8 \times 8 \times 8$   $\Gamma$ -centered  $k$ -point mesh. Structural optimization was performed starting from the primitive cell of the experimentally determined  $Fdd2$  structure with fully occupied interstitial MnA sites. Spin-orbit coupling was neglected during structural optimization, and all Mn spins were aligned ferromagnetically. The unit cell and atomic positions were optimized until the magnitude of the forces on all atoms was less than 0.001 eV/Å. Calculations including the effects of spin-orbit coupling, with noncollinear spin enabled, were then performed as single-point calculations without any further structural optimization.

Differential scanning calorimetry (DSC) data were collected using a Netzsch Pegasus 404 instrument with a Pt furnace attachment. Single crystals were placed in alumina crucibles and heated from 50 °C to 300 °C with a heating and cooling rate of 10 °C/min under a 20-mL/min flow of nitrogen.

## III. RESULTS AND DISCUSSION

### A. Synthesis and structure

Single crystals of  $\text{Mn}_{1.05}\text{Bi}$  were grown using a Bi flux technique by using a Bi:Mn ratio of 8:2 and slowly cooling from 800 °C to 430 °C in carbon coated quartz tubes, followed by centrifugation and quenching. Powder diffraction of the resulting solids showed a combination of NiAs-type  $\text{MnBi}$ ,  $\text{Mn}_{1.05}\text{Bi}$ , and Bi metal. Single crystal diffraction of the large (>20 mg) hexagonal crystals showed them to not be NiAs-type  $\text{MnBi}$  but to have an orthorhombic structure with a large unit cell. This was repeated on multiple pieces of the large crystals, with no evidence of single crystals of NiAs-type  $\text{MnBi}$ . Removal from the furnace at temperatures lower than 430 °C led to a higher fraction of NiAs-type  $\text{MnBi}$  in the powder mixture, whereas higher temperature led to a lack of precipitation of crystals. Single crystals were mechanically separated from the mixture and energy dispersive x-ray spectroscopy was performed to confirm the stoichiometry of the single crystals. Multiple measurements of the composition confirmed the Mn content in excess of 1:1; from EDX the stoichiometry is  $\text{Mn}_{1.08(4)}\text{Bi}$  with no other elements detected. The metastability of the crystals were probed by differential scanning calorimetry [38] (Fig. S5), which showed irreversible degradation of the material when heated above room

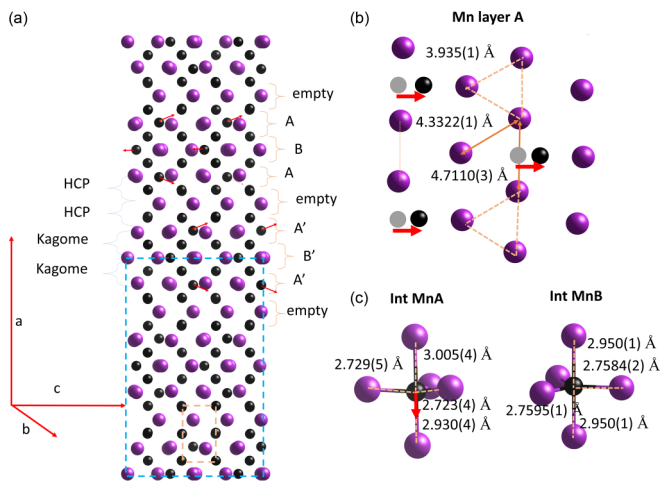


FIG. 1. (a) Structure of  $Fdd2$   $Mn_{1.05}Bi$ , with Mn atoms in black and Bi atoms in purple. The NiAs-type hexagonal unit cell is shown in the orange dotted lines and the  $F21/m1$  (an unconventional setting of  $C2/m$ ) NiBi-type unit cell is shown in the blue dotted lines. Different interstitial TB-Mn layers are indicated as  $A$ ,  $B$ ,  $A'$ ,  $B'$ , or empty. Red arrows show the displacement direction off center of the interstitial Mn atoms. The different O-Mn layers are indicated as hcp and Kagome-type layers. (b) Bi layer with interstitials filled, showing how the Bi network condenses into trimers as they move away from the interstitial TB-Mn atoms, and the in-plane off centering of the interstitial Mn atoms with respect to the pseudo-hexagonal Bi lattice. The centric positions of Mn are shown in gray spheres. (c) Coordination environment of interstitial TB-Mn in layer  $A$  and layer  $B$ , with the difference in bond lengths showing the slight off centering of the TB-Mn atom within the trigonal prism in layer  $A$ —these are again highlighted by the direction of the red arrow.

temperature. Indeed, over long periods of time ( $>3$  months) the crystals irreversibly degrade at room temperature, producing metallic Mn, MnO, and hexagonal NiAs-type MnBi.

Pieces of larger crystals were used to obtain single crystal diffraction. Details of the crystal structure solution are shown in the Supplemental Material (Tables S1–S3). The composition from single crystal diffraction was  $Mn_{1.045(3)}Bi$  due to the inclusion of ordered Mn interstitials, which is within error of the EDX stoichiometry. The material with all crystallographically distinct Mn sites fully occupied would have the composition  $Mn_{1.065}Bi$ ; the deviation from this stoichiometry is due to a refined 14(1)% vacancy of one of the Mn sites. This vacancy content was stable to refinements across multiple crystals. For purposes of discussion this will be rounded to the formula  $Mn_{1.05}Bi$ .

$Mn_{1.05}Bi$  is isostructural to  $Mn_{1.05}Rh_{0.02}Bi$ , with a space group of  $Fdd2$  and a large unit cell of  $a = 47.577(3)$  Å,  $b = 8.6499(6)$  Å and  $c = 14.957(1)$  Å (Fig. 1) at 150 K. The  $Fdd2$  space group was unambiguously preferred over  $Fddd$  and  $F222$  by the intensity statistics on five times redundant single crystal data. Furthermore, the  $Fdd2$  space group is the only space group in its Laue group that is a subgroup of the NiAs  $P6_3/mmc$  space group. The structure is composed of NiAs-type MnBi layers, with octahedrally coordinated Mn (here-on referred to as O-Mn), as well as ordered interstitial Mn sites in between the layers, with trigonal bipyramidal

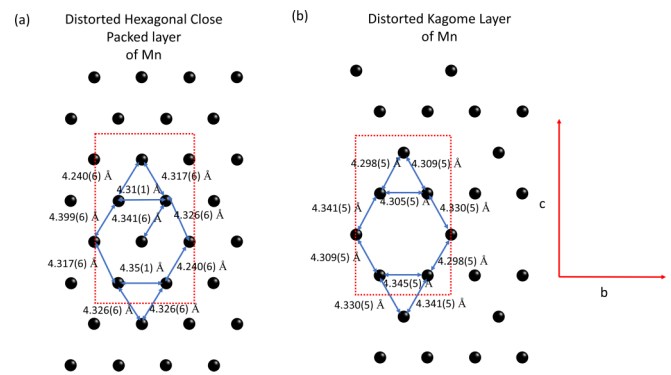


FIG. 2. A comparison of the two types of layers of O-Mn in  $Mn_{1.05}Bi$ , the (a) hexagonal close-packed-type layer and (b) Kagome-type layer obtained by ordered 25% vacancies from a hexagonal close-packed layer, as indicated in the structure in Fig. 1. Both layers are distorted away from hexagonal in the crystal structure. The unit cell is shown in red dotted lines. The distortion is highlighted by the unequal bond lengths that make up the pseudo-hexagonal Mn-Mn distances in plane.

coordinated Mn (TB-Mn) [Fig. 1(a)]. The NiAs-type layers alternate between completely filled and 25% vacant layers. The filled layers exhibit a pseudo-hexagonal close-packed (hcp) arrangement of Mn. The 25% vacant layers are nearest to the Mn interstitials, and the 25% vacancies are ordered within the layer, leading to an orthorhombically distorted Kagome motif. Thus, the octahedrally coordinated Mn exhibit an “hcp-hcp-Kagome-Kagome-type stacking” (Figs. 1 and 2).

The interstitial TB-Mn atoms are ordered within the layer, creating an orthorhombically distorted hcp arrangement of TB-Mn with twice the in-plane Mn-Mn distance as the NiAs-type O-Mn (Fig. 1). One-third of these interstitial layers are empty, and the filled interstitial layers shift relative to each other upon moving along the stacking direction, leading to  $A$ - $B$ - $A$ -type stacking followed by a layer with no interstitials. The next set of interstitials is shifted over by half the NiAs-type unit cell, leading to another  $A'$ - $B'$ - $A'$  stacking, meaning the unit cell generally has an empty- $A$ - $B$ - $A$ -empty- $A'$ - $B'$ - $A'$ -empty layer stacking, which makes up the primitive unit cell (Fig. 1). The TB-Mn interstitial sites in the  $A$  layer (int MnA), from the single crystal refinement, have only a 86(1)% occupancy of Mn, whereas those in  $B$  layers (int MnB) are within error of 100% filled. A structure with fully occupied sites in the  $A$  layer would have the composition  $Mn_{1.0625}Bi$ .

This overall structure is analogous to that found in  $Mn_{1.05}Rh_{0.02}Bi$ , with the same hcp-hcp-Kagome-Kagome stacking of the octahedral Mn, and the empty- $A$ - $B$ - $A$ -empty- $A'$ - $B'$ - $A'$ -empty stacking of the interstitial Mn. However, there are two key differences. In  $Mn_{1.05}Rh_{0.02}Bi$ , the  $B$ -layer interstitial TB-Mn is partially substituted with Rh, and the TB-Mn in the  $A$  layer is 100% occupied. This small difference in interstitial site occupancy is seemingly enough to thermodynamically stabilize the phase, and also may affect the magnetic properties due to the presence of the nonmagnetic Rh atom. The interstitial MnA and MnB atoms are both displaced in plane from the surrounding pseudo-hexagonal Bi atoms [Fig. 1(b)], with the MnA atoms displaced along  $c$ , and the MnB atoms displaced in the opposite direction. The

unequal number of these sites (with the multiplicity of the MnA site being twice that of MnB) create net electronic polarization along the  $c$  axis, which is perpendicular to the stacking axis, resulting in the polar  $Fdd2$  space group; a nonpolar space group is not compatible with the simultaneous presence of interstitial TB-Mn in an odd number of layers. Therefore,  $\text{Mn}_{1.05}\text{Bi}$  demonstrates that NiAs derivatives can be a class of polar metals that can generate polar magnetic metals.

It is notable that the polarity of  $\text{Mn}_{1.05}\text{Bi}$  is intrinsic to the ordering and coordination environment of the interstitial Mn, rather than being due to an ordered polar displacement of an atom within a coordination polyhedron, which is the typical way polar materials are described. This ordering-induced polarity has also been observed in the room-temperature polar magnetic metal  $(\text{Fe}_{0.5}\text{Co}_{0.5})_5\text{GeTe}_2$  [39]. Unlike in polar metals with a polar atomic displacement, such as  $\text{LiOsO}_3$  [40] and materials in the LiGaGe family [41], the structural feature that induces polarity in  $\text{Mn}_{1.05}\text{Bi}$  does not compete with the metallicity. Also, unlike  $\text{WTe}_2$  [42], there is little to no prospect of switchability in  $\text{Mn}_{1.05}\text{Bi}$ , even if the metallicity could be overcome as the activation barrier of moving Mn from one trigonal bipyramidal site to the next, to switch the in-plane polarization of a layer, would be much larger than reversing the polar displacement of an atom within a polyhedron. However, polar metals wherein the polarity is intrinsic to the structure, such as the TaAs family of materials, can still demonstrate interesting properties such as a giant anisotropic nonlinear optical response [43]. Overall, the fact that certain orderings of interstitials in an hcp layer are intrinsically polar, and that the ordering of these interstitial layers can lead to a net polarity for the unit cell, may be a generalizable method for synthesizing polar metals in intermetallics with HCP nets and the capacity to host interstitial ions.

The environment of the Mn interstitial itself depends on the layer it is in—the interstitial TB-Mn atoms that are in layer A (and therefore are adjacent to an empty layer) are also shifted off center along the  $a$  axis from their trigonal bipyramid towards the empty layer [Fig. 1(c)]. These same considerations exist for  $\text{Mn}_{1.05}\text{Rh}_{0.02}\text{Bi}$ , for which Rh preferentially substitutes at the Mn in layer B. The crystal structure of  $\text{Mn}_{1.05}\text{Bi}$  could not be solved in the space group  $Fddd$  without large ( $>20 e^-$ ) peaks in the electron density that could not be accounted for, nor stably refined as partially occupied Mn, further supporting the assignment of the  $Fdd2$  space group.

The presence of the TB-Mn interstitials also fundamentally alters the possible magnetic exchange pathways, as it creates new Mn-Mn interactions. In NiAs-type MnBi, there are two main Mn-Mn distances, the in-plane distance [4.285(3) Å] and out-of-plane distance [3.056(1) Å] connecting the layers. Because the TB-Mn interstitials are between the layers, their presence adds a Mn-Mn distance of 2.89(1) Å that has both in-plane and out-of-plane vector components. Furthermore, the presence of ordered vacancies in half of the NiAs-type layers, which create a Kagome motif, could lead to in-plane frustration. The TB-Mn atoms in the interstitial A layer are in a highly asymmetric environment, as they are proximate to an hcp-type O-Mn layer on one side and a Kagome-type O-Mn layer on the other. These factors are likely what contributes to the huge anisotropy and slow spin dynamics described later.

The presence of Mn interstitials in between the layers also distorts the hexagonal Bi lattice. In those layers, the Bi atoms move away from the interstitial Mn to accommodate them, leading to condensation of the lattice into trimers with a shorter Bi-Bi distance and lone Bi atoms that are only bound to O-Mn but no interstitial TB-Mn [Fig. 1(b)]. This leads to three different Bi-Bi distances within the layer—the intertrimer distance [4.7110(3) Å], the intratrimer distance [3.935(1) Å], and the distance between the lone Bi and the trimer [4.3322(1) Å].

A similar structure to  $Fdd2$   $\text{Mn}_{1.05}\text{Bi}$  has been reported for  $\text{Ni}_{1+x}\text{Bi}$  [44], which is also a defect NiAs structure in which Ni atoms migrate from the octahedral NiAs layer into the interstitial, leaving behind alternating Kagome and hcp layers of O-Ni. However, the layering in this material is different due to some disorder of the TB-Ni interstitial site, resulting in the centrosymmetric  $F12/m1$  (a different setting of  $C2/m$ ) space group, which is also roughly half the size of the unit cell observed here, due to a halved (long-axis) stacking axis. The doubling of the long axis in  $\text{Mn}_{1.05}\text{Bi}$  compared to NiBi is apparent in observable reflections along that axis that are forbidden in the NiBi unit cell. Structurally, this results from the alternating up/down displacements of the TB MnA sites, which, while small, are not within error [Fig. 1(c)]. Thus,  $\text{Mn}_{1.05}\text{Bi}$  conclusively has a different defect order from NiBi. This indicates that careful attention to site ordering in defect NiAs-type structures can result in markedly different properties, including the presence or absence of Kagome layers and inversion centers.

## B. DC magnetization

To understand the effect of this change in symmetry and structure on the magnetic properties, the DC magnetization was measured as a function of temperature, with the field applied both along the stacking axis ( $a$  axis) as well as within the layer plane (the  $bc$  plane) of the crystal structure [Fig. 3(a)]. Due to in-plane twinning (which, from the single crystal data, occurs on the submillimeter scale), the  $b$  and  $c$  directions could not be distinguished on the  $>1$ -mm size single crystals—multiple measurements within the  $bc$  plane showed the same results, meaning the magnetic anisotropy within this plane is minimal in the as-grown crystals.  $\text{Mn}_{1.05}\text{Bi}$  is known to order ferromagnetically well above 300 K, with its Curie point inaccessible due to it being above the decomposition temperature [44]. For reference,  $\text{Mn}_{1.05}\text{Rh}_{0.02}\text{Bi}$  orders ferromagnetically at 430 K. For  $\text{Mn}_{1.05}\text{Bi}$  at  $H = 1000$  Oe, the magnetization shows large anisotropy across the whole temperature range, with the magnetization along  $a$  consistently more than an order of magnitude larger than that along the  $bc$  plane (at 300 K and 1000 Oe, an 18-fold larger magnetization along  $a$  than in  $bc$  is observed). This contrasts with hexagonal NiAs-type MnBi, in which the magnetization is marginally larger along the stacking axis at room temperature, before undergoing a spin-reorientation transition changing the easy axis to the in-plane direction [21]. This indicates that in  $\text{Mn}_{1.05}\text{Bi}$ , the spin direction is effectively pinned to the out-of-plane direction ( $a$  axis).

This can be, at least partly, attributed to the interstitial Mn atoms, which create an additional exchange pathway.

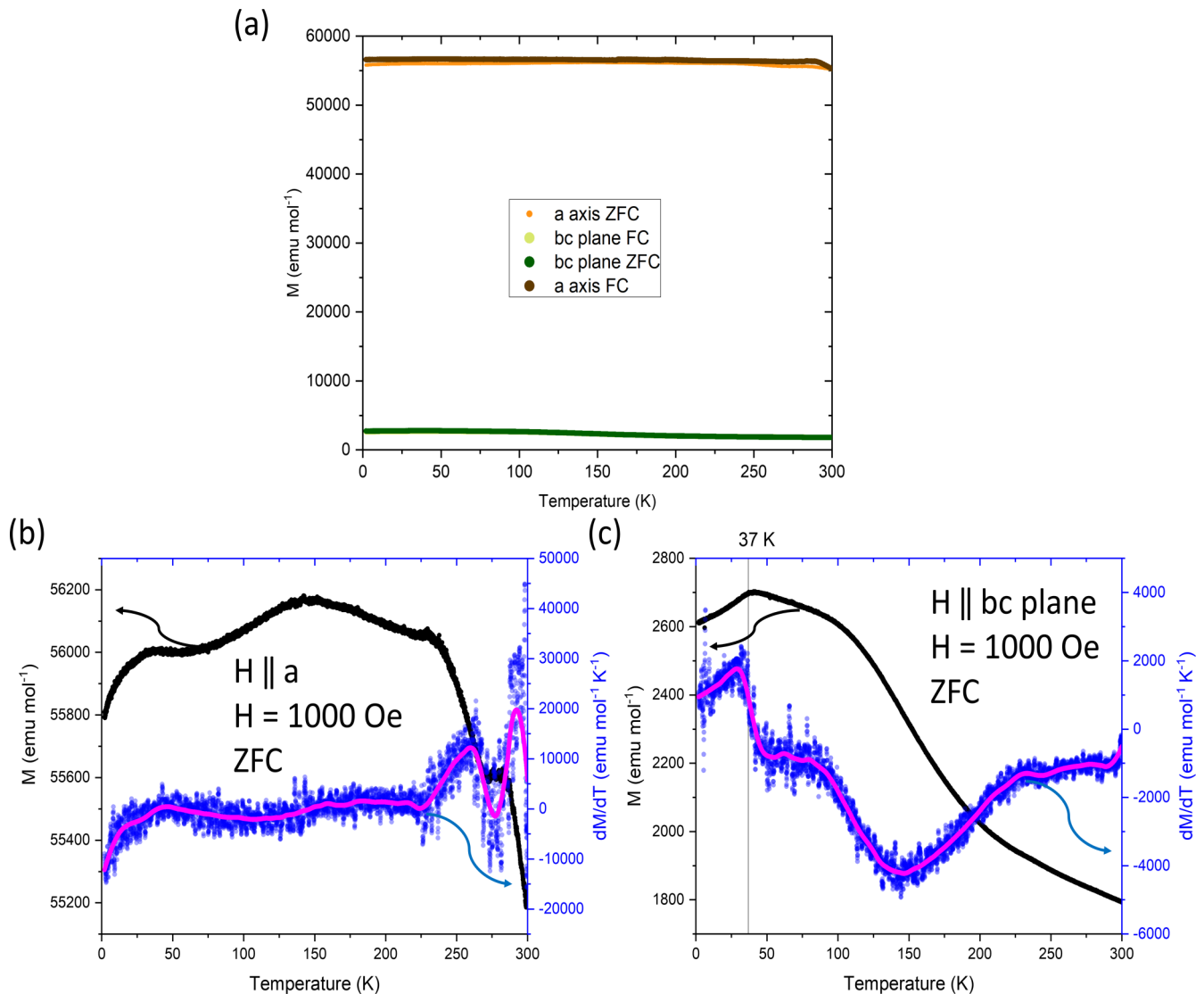


FIG. 3. (a) DC magnetization at  $H = 1000$  Oe as a function of temperature for both the stacking direction ( $a$  axis) and in-plane direction ( $bc$  plane), with both the zero field-cooled (ZFC) and field-cooled (FC) curves plotted. (b) Detailed view of the ZFC plot for the  $a$  axis along with the derivative (blue) and smoothed derivative (purple) for comparison. (c) Detailed view of the ZFC plot for the  $bc$  plane along with the derivative (blue) and smoothed derivative (purple) for comparison.

For example, in the  $\text{Mn}_{1+x}\text{Sb}$  family of materials, the excess Mn forms in similar TB-Mn interstitials but are globally disordered, leading to retention of the  $P6_3/mmc$  space-group symmetry [45]. As a function of  $x$ , the Curie temperature and the spin-reorientation temperature both decrease in magnitude, meaning that TB-Mn interstitials, even in the absence of any global symmetry change, reduce the preference for the spins to be oriented in plane [46,47].

Both magnetization curves are only weakly temperature dependent, and there is almost no difference between the field-cooled and zero-field curves. The zero-field curves are shown in more detail in Figs. 2(b) and 2(c). While the  $a$ -axis curve is very weakly temperature dependent it does show small cusps at 279, 260, and 42 K; these features correspond to peaks in the derivative, also shown for comparison. While the temperature dependence is weak, these features are well resolved and above the threshold of noise. Therefore, there

appear to be subtle transitions at these temperatures. These transitions do not appear to have been observed in NiAs-type MnBi or  $\text{Mn}_{1.05}\text{Rh}_{0.02}\text{Bi}$ ; however, further investigation of  $\text{Mn}_{1.05}\text{Rh}_{0.02}\text{Bi}$  is warranted to confirm this. For the in-plane  $bc$  direction, a broad hump centered around 150 K is observed in the derivative, as well as the peak in the derivative at 42 K that corresponds to a cusp in the magnetization. This indicates that the feature at 42 K is present in both directions, whereas the 279 and 260 K transitions are specific to the out-of-plane direction.

The transition at 260 K observed in the DC magnetization along the  $a$  axis is also observed in the  $a$ -axis AC susceptibility (see Fig. 6) and may be present in the resistivity (though it is within the threshold of noise; see Fig. 9). The 279 K transition observed in the out-of-plane DC magnetization is present in the resistivity. The lower-temperature 42 K transition is present in the out-of-plane AC susceptibility as a divergence

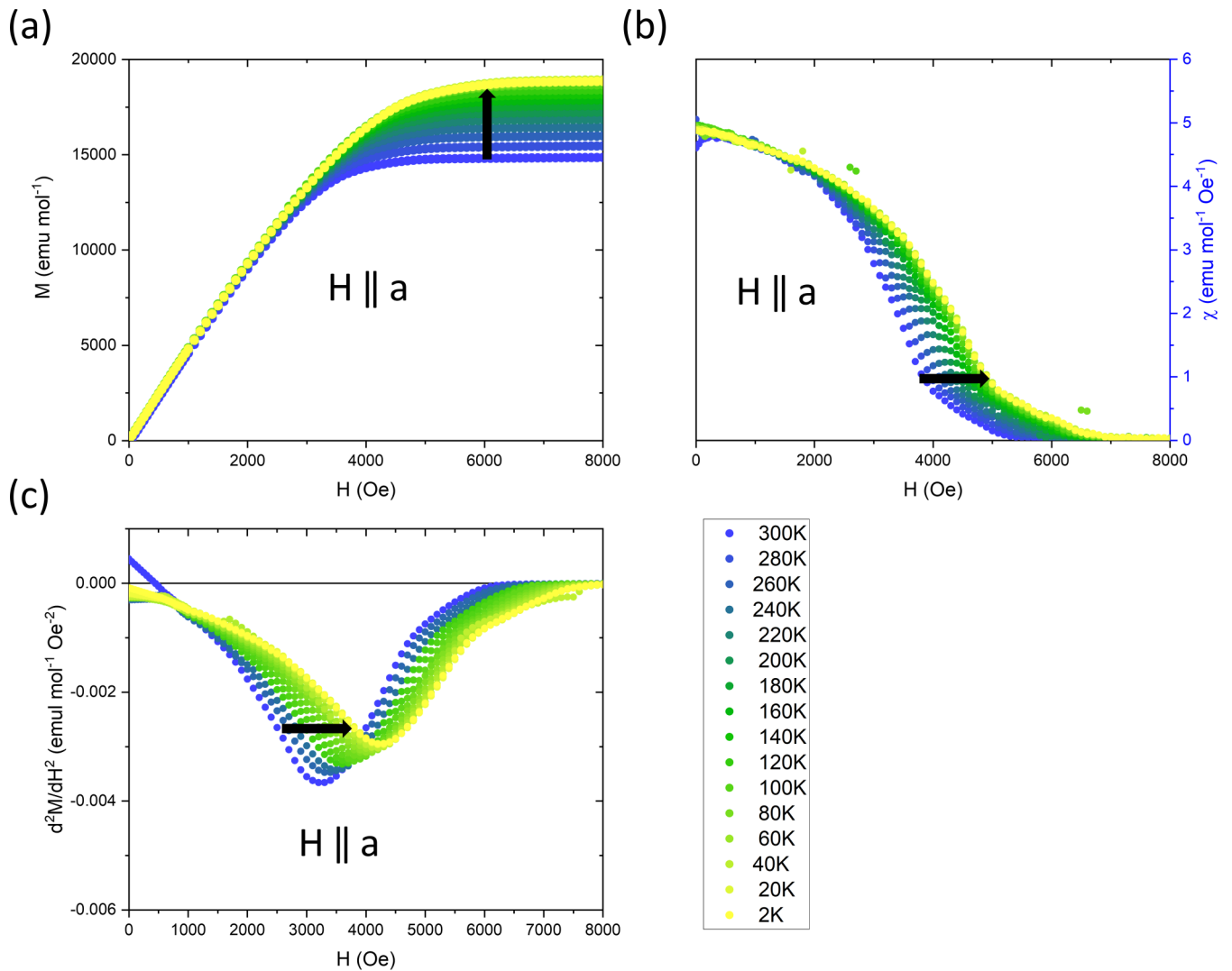


FIG. 4. (a) Magnetization vs applied field curves for the *a* axis, from 300–2 K. (b) Susceptibility versus applied field curves for the *a*-axis, from 300–2 K. (c) Derivative of the susceptibility with respect to field vs applied field curves for the *a* axis, from 300–2 K.

of the different frequency curves, which also associated with a peak in the derivative of the AC susceptibility at 35 K at 900 Hz, which is near the 42 K transition observed in the DC magnetization (Fig. S3). This feature is also present in the resistivity [see Fig. 8(b)]. The DC magnetization along both *a* and in the *bc* plane, AC magnetization and resistivity data unambiguously demonstrate features at 42 and 279 K, and the DC magnetization and resistivity show features at 42, 260, and 279 K.

To further probe the DC magnetization, magnetization versus field curves were collected for both directions in the range 2–300 K. The data for the *a* axis [Fig. 4(a)] shows ferromagnetic behavior across the whole temperature range, with the saturated magnetization increasing upon cooling with a saturating field of around 5000 Oe. The saturated magnetization at 2 K corresponds to  $3 \mu_B/\text{Mn}$  and  $2.5 \mu_B/\text{Mn}$  at 300 K, which is less than that of NiAs-type MnBi of  $4 \mu_B/\text{Mn}$  but consistent with previous reports for polycrystalline “Mn<sub>1.08</sub>Bi” (which we expect to actually be Mn<sub>1.05</sub>Bi) and Rh-doped Mn<sub>1.05</sub>Rh<sub>0.02</sub>Bi [26,28]. No hysteresis was observed in the curves, which is indicative of a well-behaved single-domain

ferromagnet, and is consistent with highly anisotropic ferromagnets. The field derivative of the magnetization, or the susceptibility [Fig. 3(b)], shows the same value within error at all temperatures at low fields ( $H < 2000$  Oe) and high fields ( $H > 8000$  Oe), but demonstrates a stronger temperature dependence at intermediate fields ( $2000 \text{ Oe} < H < 8000$  Oe), due to the change in saturation magnetization as a function of temperature. The second derivative confirms this, showing a peak between 3000 and 4000 Oe that increases in field upon cooling [Fig. 3(c)]. This indicates smooth variation of ferromagnetic properties under an applied field along *a* when cooling from 300 to 2 K.

The magnetization versus field curves along the *bc* plane show considerably different behavior. The curves are all linear above about 4000 Oe, with a low-field nonlinear feature that increases with cooling [Fig. 5(a)]. Due to the very small values of magnetization of this feature ( $< 0.5\%$  of the total magnetization of the *a* axis), this may be due to a  $< 0.5\%$  impurity of NiAs-type MnBi. The size of this feature also varies sample to sample, indicating its nature as a small impurity phase rather than a bulk feature.

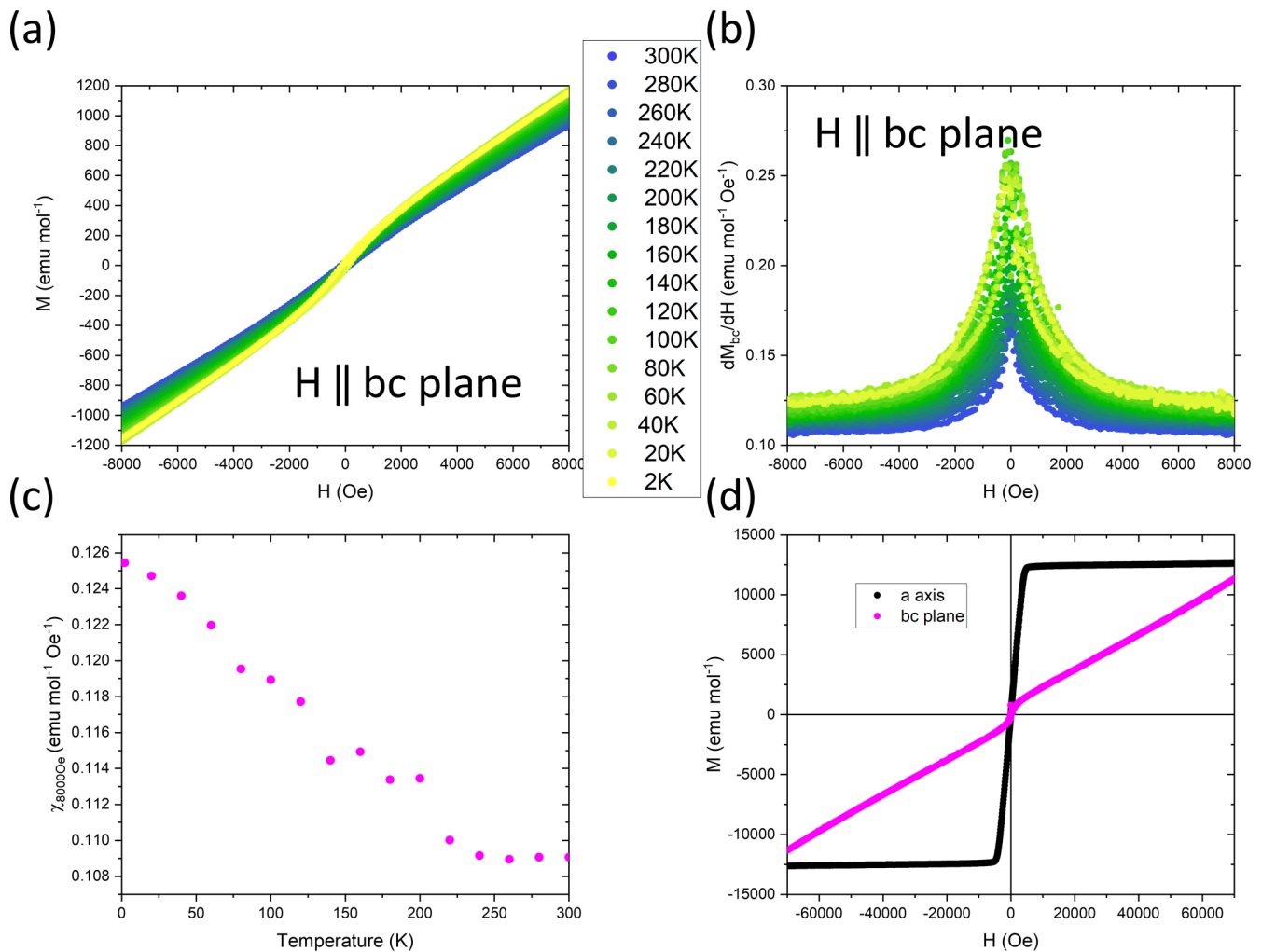


FIG. 5. (a) Magnetization vs applied field curves for the *bc* plane, from 300–2 K. (b) Susceptibility vs applied field curves for the *bc* plane, from 300–2 K. (c) Susceptibility at 8000 Oe vs temperature for the *bc* plane. (d) Direct comparison of the magnetization vs field of the *a* axis and *bc* plane, at 100 K.

Above 8000 Oe, the curves are all linear and they remain linear up to 70 000 Oe with no evidence of saturation [Fig. 4(d)]. Extraction of the susceptibility at 8000 Oe vs temperature shows a transition near 250 K [Figs. 4(b) and 4(c)], consistent with the 260 K feature observed in the constant field susceptibility. A side-by-side comparison of the in-plane and out-of-plane direction [Fig. 3(d)] demonstrates the huge anisotropy, and is consistent with that observed for  $\text{Mn}_{1.05}\text{Rh}_{0.02}\text{Bi}$ , which also has linear behavior in the in-plane direction that has not been saturated up to 70 000 Oe. This indicates at all temperatures investigated, the moment lies along the *a* axis, with an applied field in the *bc* plane leading to a small reorientation of the moments towards the *bc* plane.

### C. AC magnetization

To understand the direction- and temperature-dependent dynamics of the magnetization, AC susceptibility measurements were performed on the single crystals both along the *a* axis and in the *bc* plane. Along the *a* axis, and unlike the DC magnetization, the AC magnetization is strongly temperature dependent for both the in- and out-of-phase responses (Fig. 6).

Both responses are characterized by a sharp increase with heating from 2 K, followed by a divergence of the different frequencies and a broad peak. The susceptibility drops off with heating before a kink at 260 K, also associated with a peak in the derivative. This kink is frequency dependent as it shifts to lower temperature with lower frequency, and is also observed in the out-of-phase susceptibility, though with a harder to resolve frequency dependence. For the in-phase susceptibility, the broad peaklike feature shifts towards lower temperature with higher frequency, while for the out-of-phase response, the feature is more of a plateau that also drops off at lower temperature with higher frequencies.

It is notable that the values of the out-of-phase susceptibility are larger than 1/3 of the in-phase value. This is indicative of sluggish spin dynamics, wherein a significant fraction of the magnetization response is out of phase, even at very low frequencies of 0.5 Hz. These sluggish dynamics disappear above around 260 K as the out-of-phase value drops to zero and below about 40 K as the response drops off to a low value. This indicates that the transitions observed in the DC magnetization around 260 and 42 K are associated with the onset of these slow spin dynamics. This large increase in the

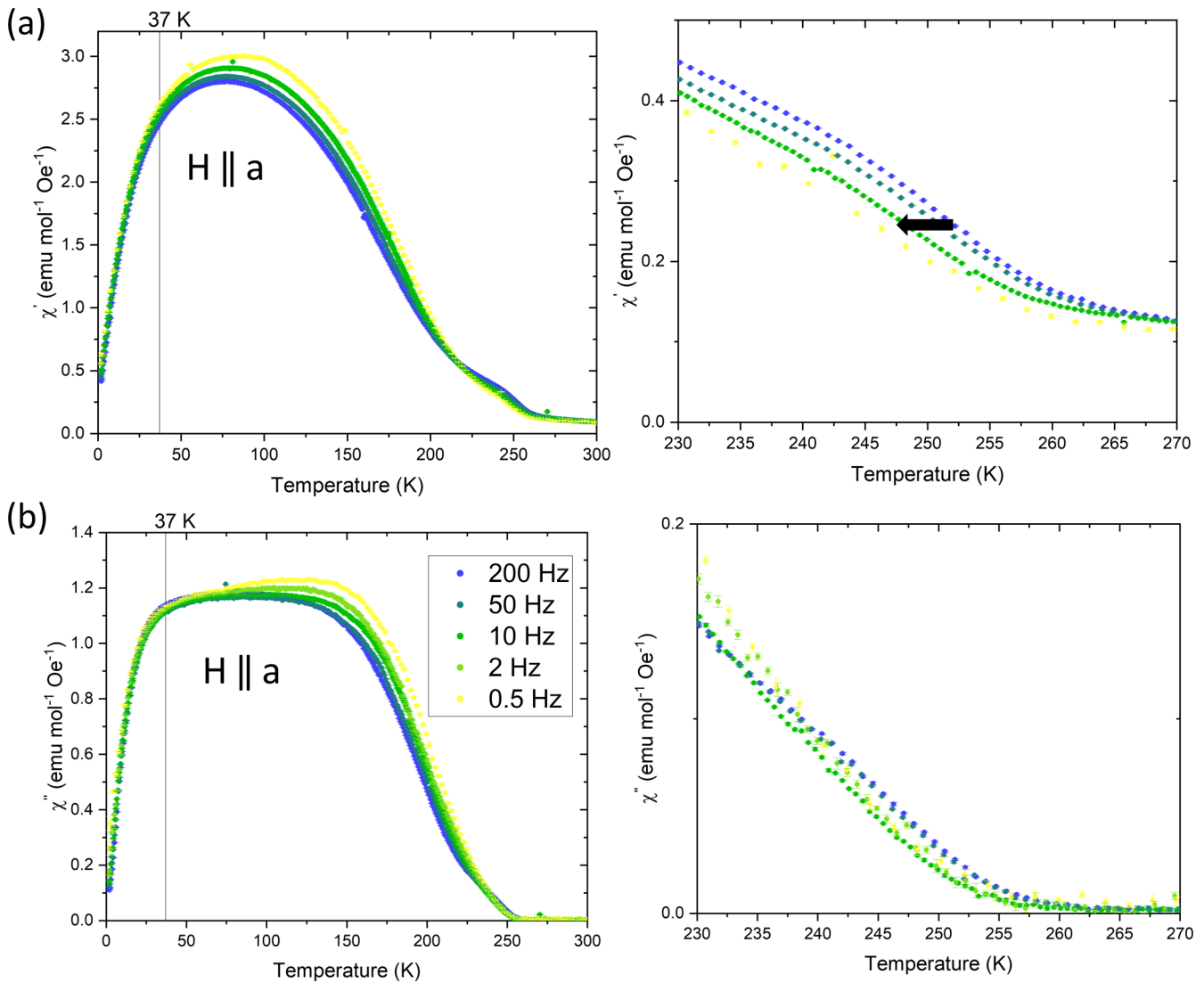


FIG. 6. Temperature dependence of the (a) in-phase AC and (b) out-of-phase AC magnetization on  $Mn_{1.05}Bi$  taken with the field applied along the  $a$  axis, at various frequencies (left) and a zoom in (right) of the high-temperature data to show the frequency-dependent transition near 260 K. An AC amplitude of 2 Oe was used for all frequencies with no applied DC bias field.

AC susceptibility, both in and out of phase, that occurs below the ferromagnetic transition temperature, is also seen in other materials such as the polar magnet  $GaV_4S_8$  and is associated with dynamics of cycloidal magnetism [48], indicating that these transitions in  $Mn_{1.05}Bi$  may involve a shift from collinear to noncollinear ferromagnetic states.

In the  $bc$  plane, the AC magnetization has a very different behavior than along the  $a$  axis (Figure 7). In phase the curves are within error independent of frequency. The temperature variation is similar to that of NiAs-type MnBi and, due to the low values of the susceptibility ( $< 10\%$  of the  $a$ -axis values), may be dominated by a small ( $< 1\%$ ) impurity of NiAs-type MnBi.

In the  $bc$ -plane out-of-phase data, a frequency-dependent feature centered around 30 K is observed; this was determined to be an artifact of the sample holder and was also observed with no sample loaded (Supplemental Material [38]). Other than this, at high frequencies, the out-of-phase susceptibility is close to zero. At lower frequencies, a hump feature emerges

centered around 150 K. While it is very noisy, the feature exists within the noise threshold. This feature is similar to that seen in the temperature derivative of the magnetization in the  $bc$  plane and may relate to a subtle change in spin dynamics with temperature that is suppressed at high frequencies. Overall, the large contribution of sluggish spin dynamics observed along the  $a$  axis is not present here and thus can be confirmed as localized along the  $a$  axis.

From the observation of multiple transitions in the DC and AC magnetizations, as well as a strongly temperature-dependent, sluggish AC response, it is clear that the magnetic structure of  $Mn_{1.05}Bi$  is complex with complex dynamics. It may indeed be the spin-spiral structure as suggested by previous literature for orthorhombic quenched polycrystalline  $Mn_{1.08}Bi$  with temperature-dependent spin fluctuations and spiral angles upon cooling from 300 K determined by powder neutron diffraction [25]. However, this study was performed on impure samples and the assignment of the spin spiral was inconclusive. However, the polycrystalline Sb-doped variant



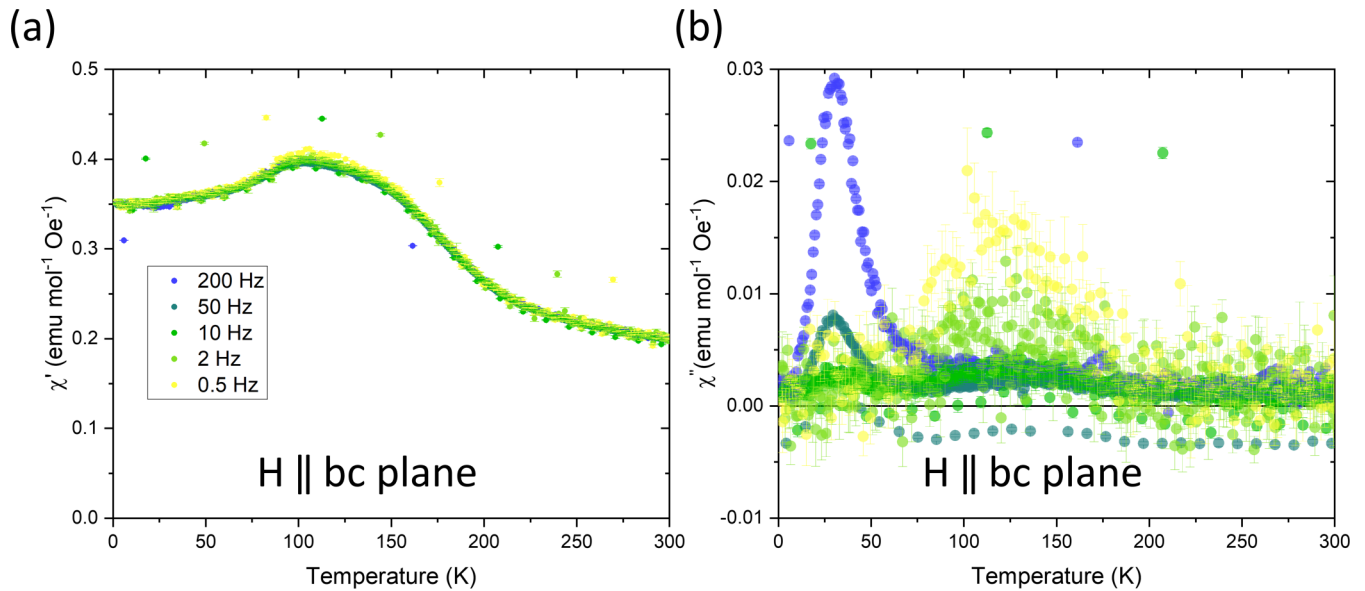


FIG. 7. Temperature dependence of the in-phase (a) and out-of-phase (b) AC susceptibility along the  $bc$  plane, at various frequencies.

$\text{MnBi}_{0.9}\text{Sb}_{0.1}$ , with assigned  $P222_1$  symmetry was phase pure and confirmed to have a spin-spiral magnetic structure [38,25]. To confirm the magnetic structure, single crystal neutron diffraction on  $\text{Mn}_{1.05}\text{Bi}$  would be helpful to reveal both the magnetic structure and dynamics.

#### D. Heat capacity

To investigate the observed magnetic transitions as well as thermodynamic properties of  $\text{Mn}_{1.05}\text{Bi}$ , heat-capacity data were measured and analyzed. The phonon contribution to the heat capacity was determined by fitting the data to a linear combination of Debye heat-capacity terms leading to an assignment of two Debye temperatures, of  $D1 = 130(5)$  K and  $D2 = 400(10)$  K, likely representing the contributions from

vibrations characteristic of Bi and Mn atoms, respectively. No peak in the heat capacity is observed in the range of 2–300 K indicating that all transitions observed in our measurements involve only small changes in entropy [(Fig. 8(a)]. The electronic term  $\gamma$  was determined by fitting the low-temperature data, starting with a  $\gamma$  term of 4.1 mJ/molK, similar to that in MnBi [21]. However, using this, an excess heat capacity was observed below 5 K; increasing  $\gamma$  to 17 mJ/molK allowed a fit to these data but at the cost of overestimating the heat capacity at high temperatures. The heat capacity also shows an upturn at low temperatures in  $C_p/T$  vs  $T^2$  curve, characteristic of a Schottky anomaly. It was then modeled using a Schottky heat-capacity term which indicates the presence of disorder, possibly leading to the existence of paramagnetic Mn centers down to 1.8 K. The energy

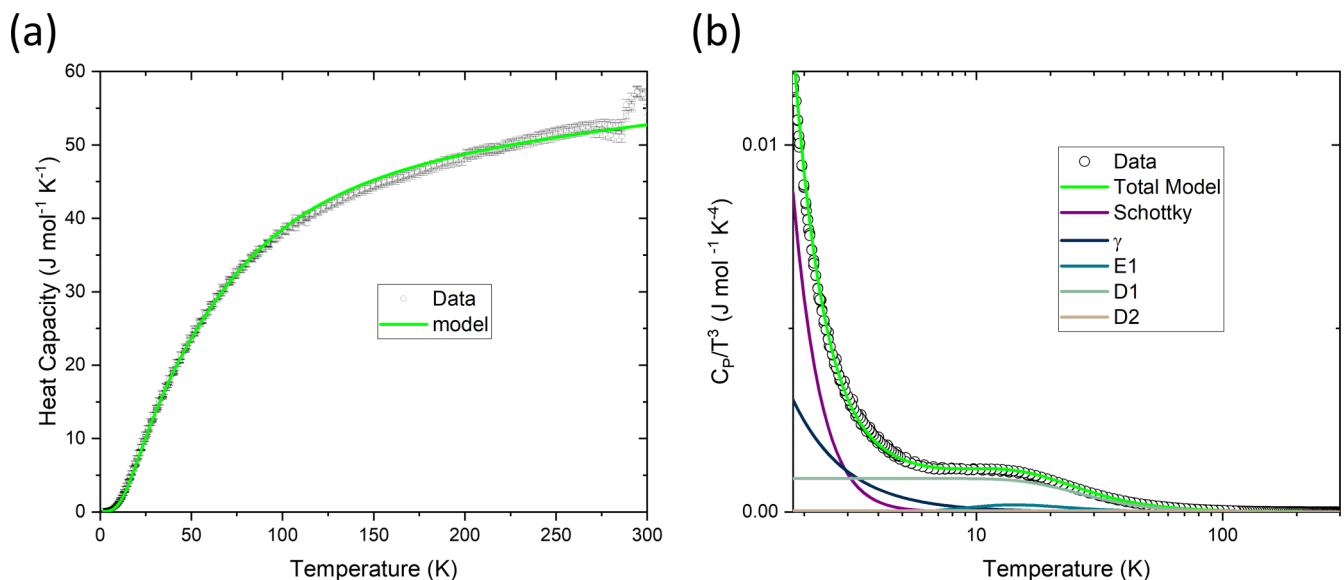


FIG. 8. (a) Heat capacity ( $C_p$ ) vs temperature of  $\text{Mn}_{1.05}\text{Bi}$ , with the model plotted on top of the data. (b)  $C_p/T^3$  vs temperature of  $\text{Mn}_{1.05}\text{Bi}$ , showing the Schottky tail and relative contributions of the Schottky, electronic, and phonon contributions.

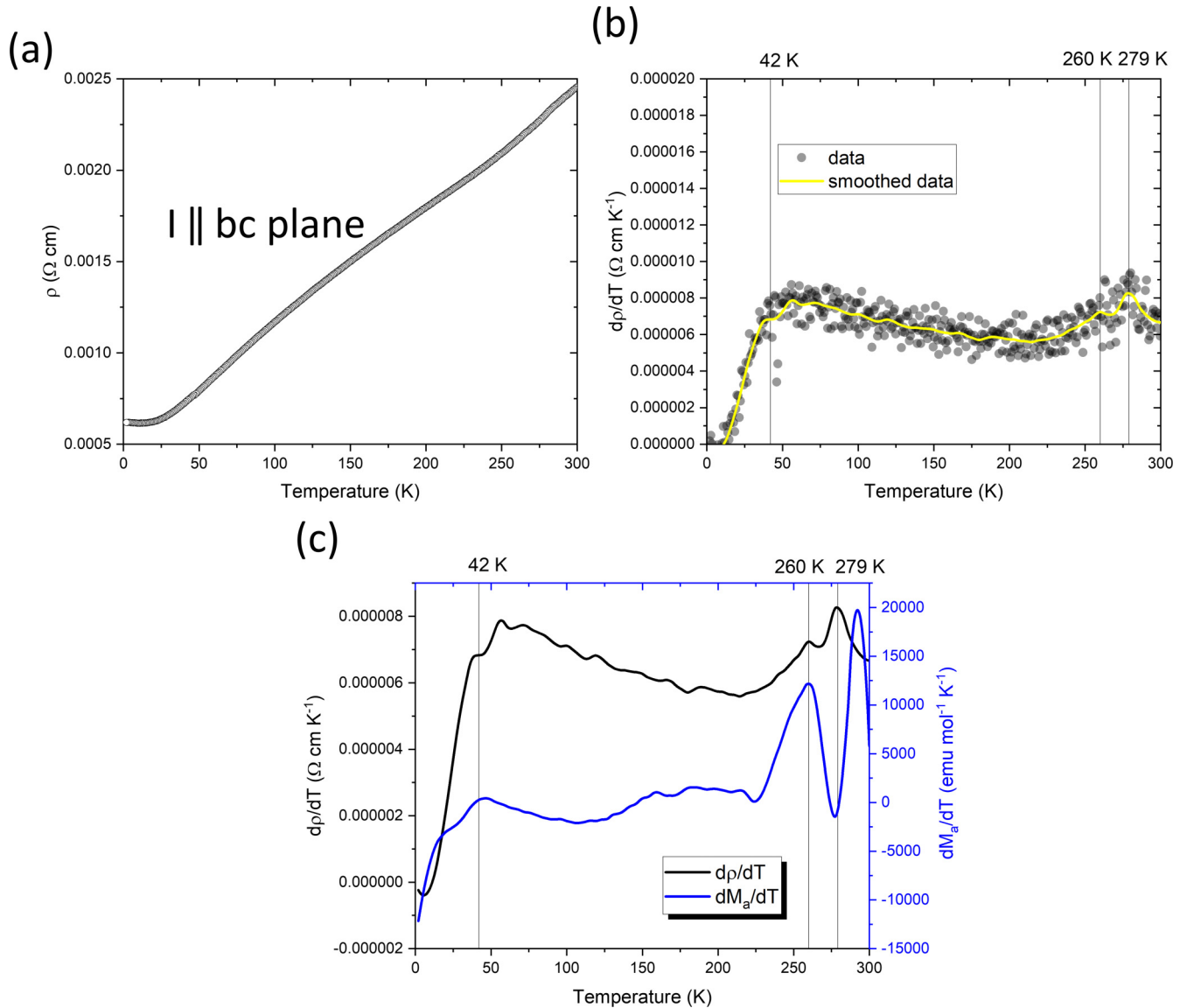


FIG. 9. (a) Resistivity of a single crystal of  $\text{Mn}_{1.05}\text{Bi}$ , with the current in the  $bc$  plane. (b) Comparison of the smoothed temperature dependence of the resistivity as well as the smoothed DC magnetization along  $a$ , showing features at 42, 260, and 279 K common to both. (c) Derivative of the resistivity and smoothed derivative of the resistivity vs temperature, showing unambiguous features at 42 and 279 K and an ambiguous feature at 260 K (within the threshold of noise).

splitting determined from the modeling of the Schottky heat capacity is estimated to be very small at a value of 3.2 K (or 0.28 meV) and a paramagnetic defect concentration of 0.02 per formula unit. The small value of the energy is likely due to the small remnant field at zero applied field. The concentration of these defect levels determined from modeling the Schottky component of 0.02 per formula unit is consistent with the refined number of Mn vacancies on the interstitial  $A$  site from the single crystal refinement, which corresponds to 0.0175(30) vacancy defects per formula unit. A fit to the data is shown as both  $C_p(T)$  vs  $T$  [Fig. 8(a)] and  $C_p/T^3$  vs  $T$  [Fig. 8(b)], the latter of which shows the relative contributions of the Schottky,  $\gamma$ , and phonon terms. A magnon term was also included, but its contribution was within the noise threshold and did not affect the other thermodynamic parameter values to within error.

The feature in the heat capacity around 290 K was determined through careful measurement using high-temperature grease to be an artifact from the grease used to affix the sample to the stage (Fig. S6). As such, no features in the heat capacity were observed above the noise threshold that relate to the 279, 260, or 42 K transitions observed via magnetization measurements, confirming that these transitions are likely then to involve minimal amounts of entropy and may be due to spin dynamics and subtle changes of spin structure.

### E. Resistivity

The resistivity was measured along the  $bc$  plane of a large single crystal [Fig. 9(a)]. The resistivity measurement shows metallic resistivity with a rather high residual resistivity of 600  $\mu\Omega$  cm and a low residual resistivity ratio (RRR) of 4.2.

TABLE I. Table showing the magnetic ordering types as well as the change in energy ( $dE$ ) from the lowest energy (noncollinear state) as well as the overall magnitude of the magnetization in various crystallographic directions of the orthorhombic  $Fdd2$  cell and the overall net magnetization.

Ordering	$dE$				$ M $
	(meV/atom)	$M_c$ ( $\mu_B$ )	$M_b$ ( $\mu_B$ )	$M_a$ ( $\mu_B$ )	
Collinear ( $a$ )	5.1	114.072	0	0	3.4
Collinear ( $b$ )	123.4	0	111.788	0	3.3
Collinear ( $c$ )	120.8	0	0	112.595	3.3
Noncollinear	0.0	94.2642	4.3132	7.6237	2.8

This is attributed to defect scattering, likely due to the Mn defects (in this case, the vacancies on the intA Mn site as refined from the single crystal data), and is in stark contrast to the low residual resistivity of  $1.6 \mu\Omega \text{ cm}$  and very large RRR of 100 for hexagonal NiAs-type MnBi crystals. A high residual resistivity is usually attributed to defects, which is consistent with the difference in crystal structure, and the apparent lack of or low concentration of Mn interstitial defects in NiAs-type MnBi. This is also consistent with the observation of the Schottky anomaly in the heat capacity.

The derivative of the resistivity closely mirrors the derivative of the DC susceptibility, as well as shows a decrease in derivative over the same temperature range as the sluggish spin dynamics as measured by the AC susceptibility [Fig. 9(b)]. This demonstrates that the temperature dependence of the resistivity is affected heavily by magnetic scattering, showing a strong coupling between the conduction electrons and magnetic moments.

#### F. Density-functional theory calculations

To better understand the properties of  $Fdd2$  MnBi, density-functional theory calculations were performed on the fully ordered  $Fdd2$  MnBi unit cell (with the assumption of no vacancies on the int MnA site, compared to the refined 14(1)% vacancy at that site from the crystal structure solution). With spin-orbit coupling included, collinear ferromagnetism along different crystallographic directions become distinct, with different energies. These are summarized in Table I. Table I shows that the energies of a ferromagnetic state that is collinear along  $b$  and collinear  $c$  are both very close to each other in energy, and about 120 meV/atom higher in energy than a ferromagnetic state that is collinear along  $a$ . This is consistent with the characterization of  $Fdd2$  MnBi as a highly anisotropic ferromagnet, with the magnetization effectively pinned along  $a$ , the stacking axis, and of the inability to distinguish between the  $b$  and  $c$  directions of the crystal from magnetization measurements.

To test for noncollinear solutions, the constraint that the magnetic solution must have orthorhombic symmetry was removed and the Mn moments were allowed to rotate. This led to a magnetic structure that was lower in energy than the solution that is collinear along  $a$ . Table I shows the energies of the various magnetic solutions as well as the magnitude of magnetization along the  $a$ ,  $b$ , and  $c$  directions. This noncollinear solution is shown in Fig. 10; the actual solution does

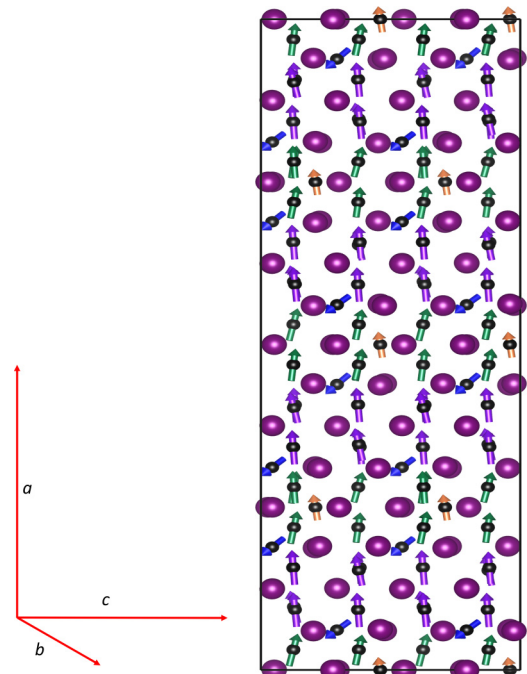


FIG. 10. Noncollinear magnetic structure solution for  $Fdd2$   $\text{Mn}_{34}\text{Bi}_{32}$  (assuming full Mn occupancy at the interstitial A site). Labels show which layers are Kagome and hcp as well as the interstitial (int) A and B sites. Arrows show both the magnitude and direction of the magnetization at each Mn site.

not retain orthorhombic symmetry, but is shown against the orthorhombic  $Fdd2$  space group for clarity. The magnitude and direction of the magnetic moment at each Mn site is shown in Table S4 (Supplemental Material). Due to computational constraints, this does not mean that this noncollinear solution is the *absolute* ground state, but does indicate that the ground state is not collinear.

In spite of these constraints, there are some features of the noncollinear state here that are important to note. While the average magnetization is overwhelmingly along the  $a$  axis, canting of the moments of the O-Mn sites is most strongly observed in the Kagome layers, hinting at the effect of magnetic frustration. Furthermore, the intA and intB sites of TB-Mn behave very differently; the intA site is canted strongly away from  $a$  while the intB site is pointed along  $a$ . The intA site is strongly asymmetric, as above it is an hcp layer of O-Mn and below a Kagome layer (whereas the intB site is between two Kagome layers); this asymmetric interaction with the Kagome layer may result in a strong spin canting or reorientation at this site. This is also consistent with the suggestion of antiparallel orientation of the moment of the interstitial sites in hexagonal NiAs-type MnBi [49]; the interstitial Tb-Mn sites therefore likely have competition between ferromagnetic and antiferromagnetic interactions with the adjacent O-Mn layers. Therefore, these calculations strongly suggest that the presence of the Kagome layers and the interstitial sites both play a role in moving  $Fdd2$  MnBi away from the collinear state. As suggested before, the real ground state may indeed be the spin-spiral ground state suggested in previous literature [49]; this should be tested by single crystal neutron

diffraction and/or further computational studies on supercells of  $\text{Mn}_{34}\text{Bi}_{32}$ .

Finally, it is notable that the magnitude of the moment of the TB-Mn on the intA and intB sites is lower on average (by about  $0.4 \mu_B$ ) than either the Kagome or hcp-type O-Mn (Table S4). This confirms that the electronic and magnetic configuration of the Mn orbitals is different on the different sites, as expected from the distinct coordination environments. This can also be expected to have an impact on the magnetic and electronic properties.

#### IV. CONCLUSION

$\text{Mn}_{1.05}\text{Bi}$  crystals, free of any third element, are grown in the space group  $Fdd2$  and characterized. The structure deviates from the parent hexagonal NiAs-type structure by ordered interstitials and ordered vacancies that leave behind Kagome layers of Mn, all resulting in a noncentrosymmetric, polar crystal structure. Thus,  $\text{Mn}_{1.05}\text{Bi}$  is a polar ferromagnetic metal at room temperature. The magnetic properties are remarkably different from the parent material MnBi;  $\text{Mn}_{1.05}\text{Bi}$  is ferromagnetic with the magnetization pinned along the stacking direction at all temperatures, with complex and sluggish spin dynamics that suggest the evolution of noncollinear or conical spin structures. DC and AC magnetization, as well as resistivity, show multiple discontinuities at the same tempera-

tures, showing these spin dynamics to be strongly temperature dependent, with multiple transitions. This is supported by calculations which suggest a noncollinear, anisotropic ground state. Overall, the inclusion of a very small amount of excess manganese to yield the single crystal composition  $\text{Mn}_{1.05}\text{Bi}$  has a drastic effect on the structure and magnetism, establishing structural features (such as Kagome layers and asymmetric Mn environments) and exchange pathways. The stabilization of this structure in single crystal form allows for measurement of these different properties. This synthesis and characterization of  $\text{Mn}_{1.05}\text{Bi}$  enables future studies on the material that probe the spin structure as well as coupling between the structural and magnetic degrees of freedom; careful control of relatively small amount of off-stoichiometry in binary intermetallics can have a profound impact on both structure and properties.

Full datasets are available at [50].

#### ACKNOWLEDGMENTS

The authors would like to acknowledge funding from the Engineering and Physical Sciences Research Council (EPSRC) Programme Grants No. EP/N004884 and No. EP/V026887). This work used the ARCHER2 UK National Supercomputing Service [51].

- 
- [1] Z. Li, J. Zhuang, L. Wang, H. Feng, Q. Gao, X. Xu, W. Hao, X. Wang, C. Zhang, and K. Wu, Realization of flat band with possible nontrivial topology in electronic kagome lattice, *Sci. Adv.* **4**, eaa4511 (2018).
- [2] M. Kang, L. Ye, S. Fang, J.-S. You, A. Levitan, M. Han, J. I. Facio, C. Jozwiak, A. Bostwick, and E. Rotenberg, Dirac fermions and flat bands in the ideal kagome metal FeSn, *Nat. Mater.* **19**, 163 (2020).
- [3] M. Kang, S. Fang, L. Ye, H. C. Po, J. Denlinger, C. Jozwiak, A. Bostwick, E. Rotenberg, E. Kaxiras, and J. G. Checkelsky, Topological flat bands in frustrated kagome lattice CoSn, *Nat. Commun.* **11**, 4004 (2020).
- [4] J.-X. Yin, W. Ma, T. A. Cochran, X. Xu, S. S. Zhang, H.-J. Tien, N. Shumiya, G. Cheng, K. Jiang, and B. Lian, Quantum-limit Chern topological magnetism in  $\text{TbMn}_6\text{Sn}_6$ , *Nature (London)* **583**, 533 (2020).
- [5] N. J. Ghimire, R. L. Dally, L. Poudel, D. Jones, D. Michel, N. T. Magar, M. Bleuel, M. A. McGuire, J. Jiang, and J. Mitchell, Competing magnetic phases and fluctuation-driven scalar spin chirality in the kagome metal  $\text{YMn}_6\text{Sn}_6$ , *Sci. Adv.* **6**, eabe2680 (2020).
- [6] H. Yang, Y. Sun, Y. Zhang, W.-J. Shi, S. S. Parkin, and B. Yan, Topological Weyl semimetals in the chiral antiferromagnetic materials  $\text{Mn}_3\text{Ge}$  and  $\text{Mn}_3\text{Sn}$ , *New J. Phys.* **19**, 015008 (2017).
- [7] T. Nakajima, H. Oike, A. Kikkawa, E. P. Gilbert, N. Booth, K. Kakurai, Y. Taguchi, Y. Tokura, F. Kagawa, and T.-h. Arima, Skyrmion lattice structural transition in MnSi, *Sci. Adv.* **3**, e1602562 (2017).
- [8] C. Pappas, E. Lelièvre-Berna, P. Falus, P. M. Bentley, E. Moskvina, S. Grigoriev, P. Fouquet, and B. Farago, Chiral Paramagnetic Skyrmion-Like Phase in MnSi, *Phys. Rev. Lett.* **102**, 197202 (2009).
- [9] J. P. Walsh, S. M. Clarke, Y. Meng, S. D. Jacobsen, and D. E. Freedman, Discovery of  $\text{FeBi}_2$ , *ACS Cent. Sci.* **2**, 867 (2016).
- [10] S. Tencé, O. Janson, C. Krellner, H. Rosner, U. Schwarz, Y. Grin, and F. Steglich,  $\text{CoBi}_3$ —the first binary compound of cobalt with bismuth: High-pressure synthesis and superconductivity, *J. Phys.: Condens. Matter* **26**, 395701 (2014).
- [11] J.-K. Bao, Z.-T. Tang, H. J. Jung, J.-Y. Liu, Y. Liu, L. Li, Y.-K. Li, Z.-A. Xu, C.-M. Feng, and H. Chen, Unique  $[\text{Mn}_6\text{Bi}_5]$ -nanowires in  $\text{KMn}_6\text{Bi}_5$ : A quasi-one-dimensional antiferromagnetic metal, *J. Am. Chem. Soc.* **140**, 4391 (2018).
- [12] Z. Liu, Q. Dong, P. Yang, P. Shan, B. Wang, J. Sun, Z. Dun, Y. Uwatoko, G. Chen, and X. Dong, Pressure-Induced Superconductivity up to 9 K in the Quasi-One-Dimensional  $\text{KMn}_6\text{Bi}_5$ , *Phys. Rev. Lett.* **128**, 187001 (2022).
- [13] C. Hu, L. Ding, K. N. Gordon, B. Ghosh, H.-J. Tien, H. Li, A. G. Linn, S.-W. Lien, C.-Y. Huang, and S. Mackey, Realization of an intrinsic ferromagnetic topological state in  $\text{MnBi}_8\text{Te}_{13}$ , *Sci. Adv.* **6**, eaba4275 (2020).
- [14] J.-Q. Yan, Y. Liu, D. Parker, Y. Wu, A. Aczel, M. Matsuda, M. McGuire, and B. Sales, A-type antiferromagnetic order in  $\text{MnBi}_4\text{Te}_7$  and  $\text{MnBi}_6\text{Te}_{10}$  single crystals, *Phys. Rev. Mater.* **4**, 054202 (2020).
- [15] A. F. May, M. A. McGuire, and B. C. Sales, Effect of Eu magnetism on the electronic properties of the candidate Dirac material  $\text{EuMnBi}_2$ , *Phys. Rev. B* **90**, 075109 (2014).
- [16] A. Zhang, C. Liu, C. Yi, G. Zhao, T.-I. Xia, J. Ji, Y. Shi, R. Yu, X. Wang, and C. Chen, Interplay of Dirac electrons and magnetism in  $\text{CaMnBi}_2$  and  $\text{SrMnBi}_2$ , *Nat. Commun.* **7**, 13833 (2016).
- [17] B. Saparov and A. S. Sefat, Crystals, magnetic and electronic properties of a new  $\text{ThCr}_2\text{Si}_2$ -type  $\text{BaMn}_2\text{Bi}_2$  and K-doped compositions, *J. Solid State Chem.* **204**, 32 (2013).

- [18] N. Janša, K.-K. Huynh, T. Ogasawara, M. Klanjšek, P. Jeglič, P. Carretta, K. Tanigaki, and D. Arčon, Electron correlations and charge segregation in layered manganese pnictide antiferromagnets showing anomalously large magnetoresistance, *Phys. Rev. B* **103**, 064422 (2021).
- [19] A. Pandey, P. Miao, M. Klemm, H. He, H. Wang, X. Qian, J. W. Lynn, and M. Aronson, Correlations and incipient antiferromagnetic order within the linear Mn chains of metallic  $\text{Ti}_4\text{MnBi}_2$ , *Phys. Rev. B* **102**, 014406 (2020).
- [20] E. Adams, W. M. Hubbard, and A. M. Syeles, A new permanent magnet from powdered manganese bismuthide, *J. Appl. Phys.* **23**, 1207 (1952).
- [21] M. A. McGuire, H. Cao, B. C. Chakoumakos, and B. C. Sales, Symmetry-lowering lattice distortion at the spin reorientation in MnBi single crystals, *Phys. Rev. B* **90**, 174425 (2014).
- [22] Y. He, S. Schneider, T. Helm, J. Gayles, D. Wolf, I. Soldatov, H. Borrmann, W. Schnelle, R. Schaefer, and G. H. Fecher, Topological Hall effect arising from the mesoscopic and microscopic non-coplanar magnetic structure in MnBi, *Acta Mater.* **226**, 117619 (2022).
- [23] Y. He, J. Gayles, M. Yao, T. Helm, T. Reimann, V. N. Strocov, W. Schnelle, M. Nicklas, Y. Sun, and G. H. Fecher, Large linear non-saturating magnetoresistance and high mobility in ferromagnetic MnBi, *Nat. Commun.* **12**, 4576 (2021).
- [24] B. He, C. Şahin, S. R. Boona, B. C. Sales, Y. Pan, C. Felser, M. E. Flatté, and J. P. Heremans, Large magnon-induced anomalous Nernst conductivity in single-crystal MnBi, *Joule* **5**, 3057 (2021).
- [25] A. Andresen, J. Engebretsen, and J. Refsnes, Neutron diffraction investigations on quenched MnBi and  $\text{MnBi}_{0.9}\text{Sb}_{0.1}$ , *Acta Chem. Scand.* **26**, 175 (1972).
- [26] T. Chen and W. Stutius, The phase transformation and physical properties of the MnBi and  $\text{Mn}_{1.08}\text{Bi}$  compounds, *IEEE Trans. Magn.* **10**, 581 (1974).
- [27] A. Gabay, G. Hadjipanayis, and J. Cui, Effect of Sb substitution on crystal structure, texture and hard magnetic properties of melt-spun MnBi alloys, *J. Alloys Compd.* **792**, 77 (2019).
- [28] V. Taufour, S. Thimmaiah, S. March, S. Saunders, K. Sun, T. N. Lamichhane, M. J. Kramer, S. L. Bud'ko, and P. C. Canfield, Structural and Ferromagnetic Properties of an Orthorhombic Phase of MnBi Stabilized with Rh Additions, *Phys. Rev. Appl.* **4**, 014021 (2015).
- [29] K. Lee, J. Suits, and G. Street, Stabilization of the high-temperature phase of MnBi by the addition of rhodium or ruthenium, *Appl. Phys. Lett.* **26**, 27 (1975).
- [30] H. Göbel, E. Wolfgang, and H. Harms, Properties of MnBi compounds partially substituted with Cu, Zn, Ti, Sb, and Te. I. Formation of mixed phases and crystal structures, *Phys. Status Solidi* **34**, 553 (1976).
- [31] C. Luo, S. H. Liou, L. Gao, Y. Liu, and D. J. Sellmyer, Nanostructured FePt:  $\text{B}_2\text{O}_3$  thin films with perpendicular magnetic anisotropy, *Appl. Phys. Lett.* **77**, 2225 (2000).
- [32] G. M. Sheldrick, SHELXT—Integrated space-group and crystal-structure determination, *Acta Crystallogr. A* **71**, 3 (2015).
- [33] O. V. Dolomanov, L. J. Bourhis, R. J. Gildea, J. A. Howard, and H. Puschmann, OLEX2: A complete structure solution, refinement and analysis program, *J. Appl. Crystallogr.* **42**, 339 (2009).
- [34] G. Kresse and J. Furthmüller, Efficient iterative schemes for ab initio total-energy calculations using a plane-wave basis set, *Phys. Rev. B* **54**, 11169 (1996).
- [35] P. E. Blöchl, Projector augmented-wave method, *Phys. Rev. B* **50**, 17953 (1994).
- [36] G. Kresse and D. Joubert, From ultrasoft pseudopotentials to the projector augmented-wave method, *Phys. Rev. B* **59**, 1758 (1999).
- [37] J. P. Perdew, K. Burke, and M. Ernzerhof, Generalized Gradient Approximation Made Simple, *Phys. Rev. Lett.* **77**, 3865 (1996).
- [38] See Supplemental Material at <http://link.aps.org/supplemental/10.1103/PhysRevMaterials.6.114405> for detailed discussion of the crystal structure and stability of  $\text{Mn}_{1.05}\text{Bi}$  as well as previous neutron diffraction studies on high-temperature MnBi and  $\text{MnBi}_{0.9}\text{Sb}_{0.1}$  reported in Ref. [25].
- [39] H. Zhang, Y.-T. Shao, R. Chen, X. Chen, S. Susarla, D. Raffrey, J. T. Reichanader, L. Caretta, X. Huang, and N. S. Settinieri, A room temperature polar magnetic metal, *Phys. Rev. Mater.* **6**, 044403 (2022).
- [40] Y. Shi, Y. Guo, X. Wang, A. J. Princep, D. Khalyavin, P. Manuel, Y. Michiue, A. Sato, K. Tsuda, and S. Yu, A ferroelectric-like structural transition in a metal, *Nat. Mater.* **12**, 1024 (2013).
- [41] W. Zhou and A. Ariando, Review on ferroelectric/polar metals, *Jpn. J. Appl. Phys.* **59**, SI0802 (2020).
- [42] Z. Fei, W. Zhao, T. A. Palomaki, B. Sun, M. K. Miller, Z. Zhao, J. Yan, X. Xu, and D. H. Cobden, Ferroelectric switching of a two-dimensional metal, *Nature (London)* **560**, 336 (2018).
- [43] L. Wu, S. Patankar, T. Morimoto, N. L. Nair, E. Thewalt, A. Little, J. G. Analytis, J. E. Moore, and J. Orenstein, Giant anisotropic nonlinear optical response in transition metal monopnictide Weyl semimetals, *Nat. Phys.* **13**, 350 (2017).
- [44] M. Ruck, Die kristallstruktur von BiNi: Eine komplexe ausdünnungsvariante des  $\text{MnNi}_2$ -Typs, *Z. Anorg. Allg. Chem.* **625**, 2050 (1999).
- [45] Y. Yamaguchi and H. Watanabe, Magnetic and crystallographic study on the electronic state of interstitial cations in MnSb, *J. Phys. Soc. Jpn.* **46**, 1138 (1979).
- [46] A. E. Taylor, T. Berlijn, S. E. Hahn, A. F. May, T. J. Williams, L. Poudel, S. Calder, R. S. Fishman, M. B. Stone, and A. A. Aczel, Influence of interstitial Mn on magnetism in the room-temperature ferromagnet  $\text{Mn}_{1+\delta}\text{Sb}$ , *Phys. Rev. B* **91**, 224418 (2015).
- [47] J. A. Kurzman, A. J. Martinolich, and J. R. Neilson, Influence of interstitial Mn on local structure and magnetism in  $\text{Mn}_{1+\delta}\text{Sb}$ , *Phys. Rev. B* **92**, 184414 (2015).
- [48] E. Clements, R. Das, G. Pokharel, M. Phan, A. Christianson, D. Mandrus, J. Prestigiacomo, M. Osofsky, and H. Srikanth, Robust cycloid crossover driven by anisotropy in the skyrmion host  $\text{GaV}_4\text{S}_8$ , *Phys. Rev. B* **101**, 094425 (2020).
- [49] R. Sabiryanov and S. Jaswal, Magneto-optical properties of MnBi doped with Cr, *J. Appl. Phys.* **85**, 5109 (1999).
- [50] <https://datacat.liverpool.ac.uk/1734/>.
- [51] <https://www.archer2.ac.uk>.